

Chapter 1

Theoretical Background of Thermal Infrared Remote Sensing

Claudia Kuenzer and Stefan Dech

Abstract Thermal infrared (TIR) data is acquired by a multitude of ground-based, airborne, and spaceborne remote sensing instruments. A broad variety of fields apply thermal infrared remote sensing, for example to assess general land- or sea-surface temperature dynamics, detect forest, coal and peat fires, map urban heat islands or thermal water pollution, differentiate geologic surfaces, analyze soil moisture, or even to test materials, to name only a few applications. As thermal infrared data has to be analyzed slightly differently than reflective data, this chapter contains the relevant theoretical background. The thermal domain of the electromagnetic spectrum, the laws of Planck, Stefan-Boltzmann, Wien, and Kirchhoff, as well as important parameters such as kinetic and radiance temperature, emissivity, and thermal inertia are briefly explained. The chapter thus provides readers with a common understanding before proceeding to subsequent chapters.

1.1 Introduction

All objects with a temperature above absolute zero (0 K, which equals $-273\text{ }^{\circ}\text{C}$) emit electromagnetic radiation. Our earth has an average temperature of about 300 K and its peak of electromagnetic emittance is located in the thermal infrared, TIR, domain at about $9.7\text{ }\mu\text{m}$ (Tipler 2000; Sabins 1996). The earth absorbs a large part of the incoming solar radiation and a corresponding amount is emitted at longer wavelengths.

Remote sensing sensors responsive in the thermal domain have the ability to record this TIR radiation. Radiation – as opposed to conduction or convection, where heat is transferred through matter – is an energy transfer process, which also works in/through a vacuum (Sabins 1996). TIR sensors thus enable the derivation of

C. Kuenzer (✉) • S. Dech

German Remote Sensing Data Center (DFD), Earth Observation Center (EOC),

German Aerospace Center (DLR), Oberpfaffenhofen, Germany

e-mail: Claudia.kuenzer@dlr.de

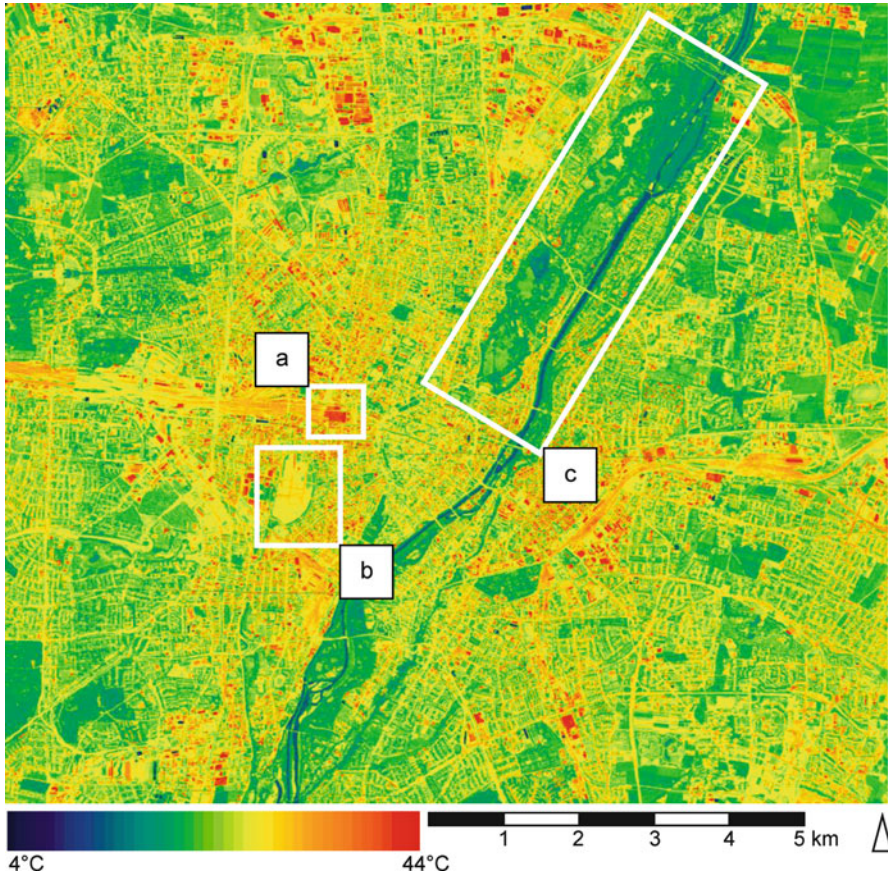


Fig. 1.1 Thermal daytime land surface temperature image of Munich, 1982, based on data acquired with an airborne Bendix Scanner. *Areas marked* include the Munich central train station (*a*), the location – a large meadow – of the annual Oktoberfest (*b*) and the southern part of the English Garden, Munich’s largest inner-city park (*c*) (Imagery courtesy of DLR)

thermal radiance images of objects on the earth’s surface. Such imagery can display the kinetic temperature of objects at the resolution of the respective sensor. The necessary correction steps for certain object-inherent as well as geometric and atmospheric effects will be addressed later in this chapter.

The most commonly known products derived from TIR imagery are land surface temperature, LST, (see Fig. 1.1) and sea surface temperature, SST (Dech et al. 1998). However, thermal data have a much larger potential than just the derivation of these standard products. These data enable the assessment of thermal anomalies (forest fires, coal fires, thermal pollution, energy leaks in buildings, inflamed areas in thermal medical imagery), the analysis of moisture conditions, or even the monitoring of machine performance in industrial applications, and – depending on sensor and resolution – the assessment of thermal dynamics at different scales (see Figs. 1.2 and 1.3).

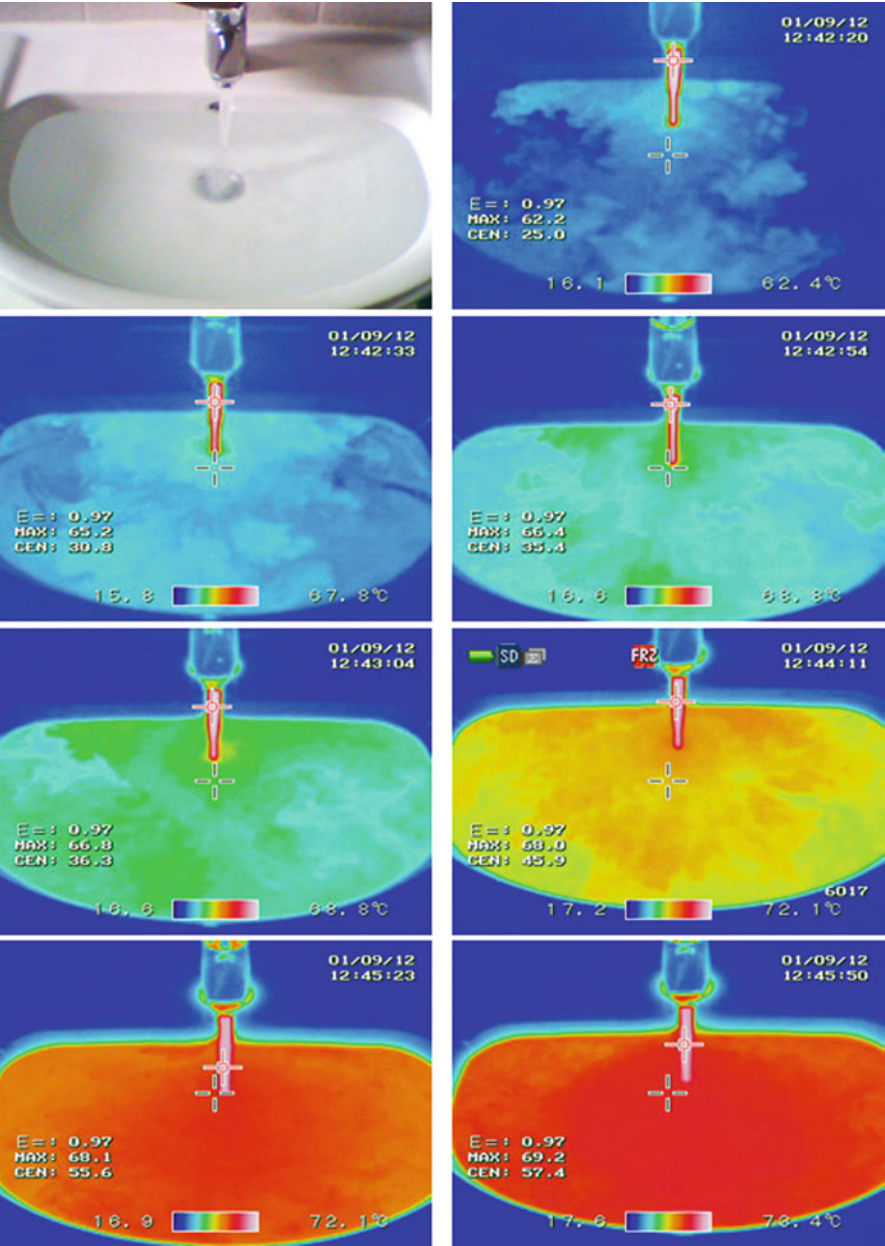


Fig. 1.2 Thermal dynamics. Hot water runs into a sink filled with colder water of 22 °C. The hot water has a temperature between 62.2 and 69.2 °C (during the course of 1 min the hot water coming from the tap increases in temperature). The mixing of the hotter into the colder water is clearly evident in the image sequence. Emissivity is set to 0.97 as water in Munich, Germany, is extremely hard at over >2.5 mmol/l CaCO₃ (Photographs: C. Kuenzer)

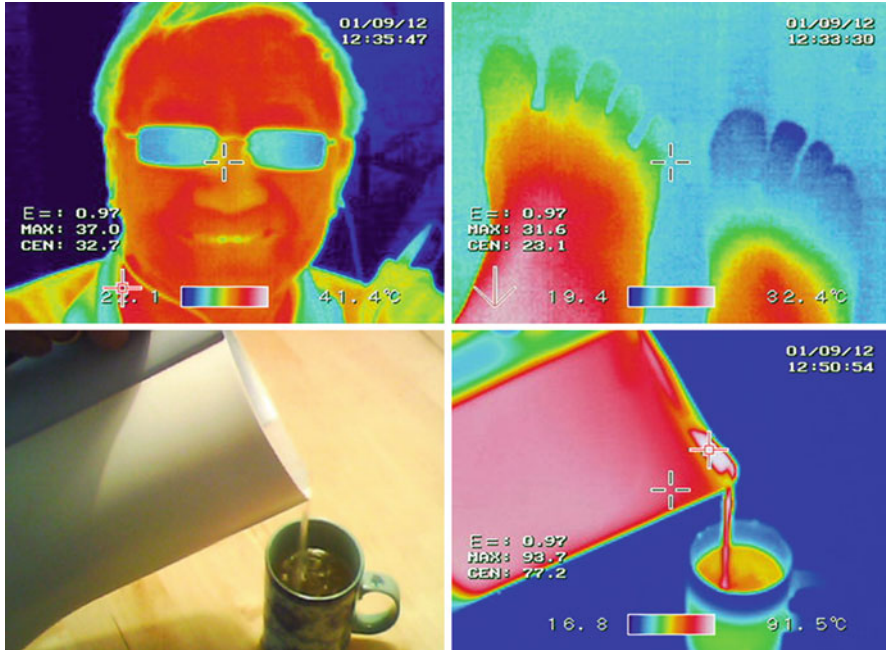


Fig. 1.3 Thermal camera images. *Upper left*: person wearing glasses. The background as well as the glasses are colder than the human skin, which has a temperature between 36 and 37 °C. *Upper right*: a male foot (*left*) and a female foot (*right*). Since blood circulation towards the toes in the female foot is less accentuated than in the male foot, the female foot appears overall colder. *Lower left*: optical image of hot water poured from an electric water kettle into a tea mug. *Lower right*: The hottest parts of this image are at the spout and in the stream of water flowing into the mug. Note the temperature increase of the mug (*green*) caused by heat conduction (Photographs: C. Kuenzer)

A broad overview of the fleet of currently available TIR sensors and the large spectrum of TIR remote sensing applications can be found in the following chapters of this book. This chapter presents the theoretical background of thermal infrared remote sensing, which must be understood to correctly analyze and interpret TIR data.

1.2 Theoretical Background

1.2.1 The Thermal Infrared Domain and Atmospheric Windows

There is no strict or physical definition of the thermal infrared domain. According to Sabins (1996) the thermal infrared wavelength domain extends from about 3 to 14 μm . In this range thermal mapping of the earth's surface is possible due

to atmospheric windows in the 3–5 μm range, as well as in the 8–14 μm range (see also Fig. 1.4 below). Within the 8–14 μm range only a narrow absorption band of ozone, O_3 , exists, which is omitted by most sensors. Within the 3–5 μm range reflected sunlight can still slightly contaminate the (emitted) thermal signal, which has to be taken into account when analyzing daytime 3–5 μm TIR imagery.

However, different authors define the TIR domain slightly differently. According to Löffler (1994) as well as Lillesand and Kiefer (1994) the TIR domain ranges from 3 to 1,000 μm . The main characteristic common to all definitions is the fact that TIR remote sensing records emitted radiation, whereas multispectral remote sensing in the visible, VIS, and near infrared, NIR, domain records reflected radiation. Only within the shorter wavelength part of the TIR spectrum (<5 μm) can the thermal signal still be slightly disturbed by reflected radiation.

1.2.2 Planck's Law

Planck's blackbody radiation law, Planck's law for short, describes the electromagnetic radiation emitted by a blackbody at a given wavelength M_λ as a function of the blackbody's absolute temperature (Planck 1900). A blackbody is defined as an (hypothetical, nonexistent) ideal radiator that totally absorbs and re-emits all energy incident upon it. Simply by specifying a certain wavelength in Eq. 1.1 below, M_λ can be calculated from the body's temperature (see also Fig. 1.5).

$$M_\lambda = \frac{2\pi hc^2}{\lambda^5 (e^{hc/\lambda kT} - 1)} \quad (1.1)$$

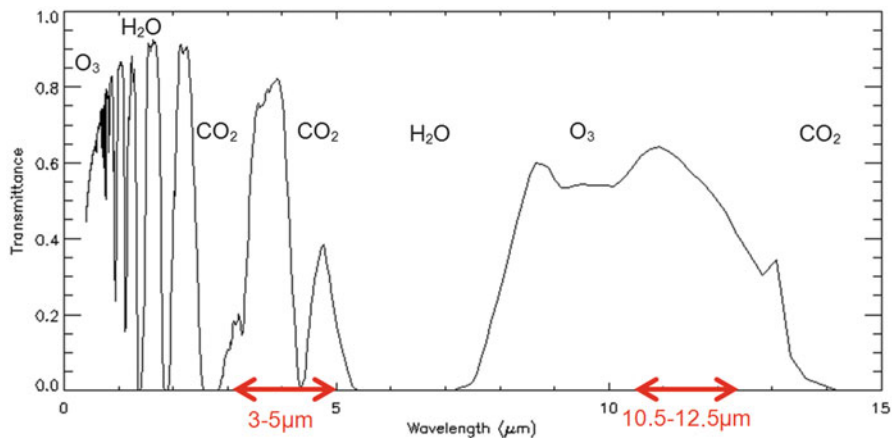


Fig. 1.4 The thermal infrared wavelength domain, typical absorption bands induced by gasses and water, and atmospheric transmittance (atmospheric windows) (Figure courtesy of Rudolf Richter)

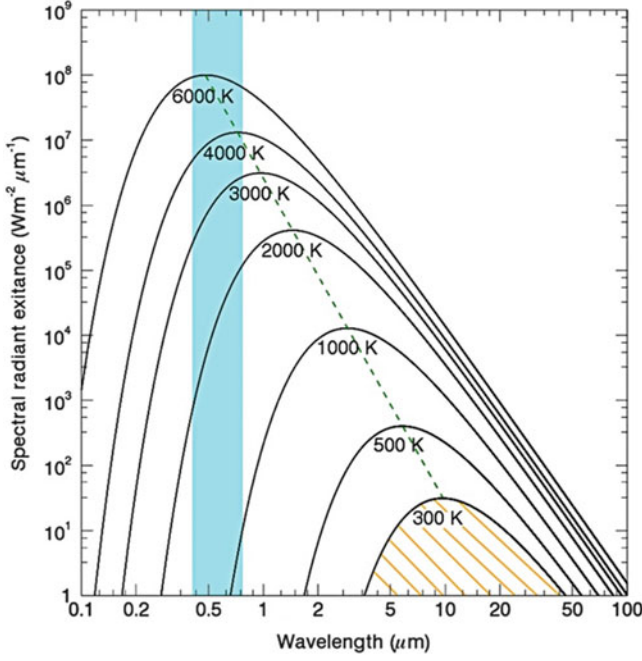


Fig. 1.5 Blackbody radiation curves at different selected temperatures, as derived from Eq. 1.1. The laws of Planck, Stefan-Boltzmann (*marked area under the 300 K curve*) and Wien (*green dotted line*) are depicted in this figure. The blue bar indicates the VIS region

with:

M_λ = spectral radiant exitance [$\text{W m}^{-2} \mu\text{m}^{-1}$]
 h = Planck's constant [$6.626 \times 10^{-34} \text{ J s}$]
 c = speed of light [$2.9979246 \times 10^8 \text{ m s}^{-1}$]
 k = Boltzmann constant [$1.3806 \times 10^{-23} \text{ J K}^{-1}$]
 T = absolute temperature [K]
 λ = wavelength [μm]

The total energy a blackbody radiates and the wavelength of maximum emittance depend on the temperature of the blackbody and can be described by Stefan-Boltzmann's law and Wien's law (Walker 2008; Tipler 2000).

1.2.3 Stefan-Boltzmann Law

The Stefan-Boltzmann law (Eq. 1.2) describes the total electromagnetic radiation emitted by a blackbody as a function of the absolute temperature of that blackbody (Walker 2008; Tipler 2000; Sabins 1996). The emitted radiation corresponds to the area under the radiation curve (integral) as depicted in Fig. 1.5.

$$T_{RadBB} = \sigma T_{kin}^4 \quad (1.2)$$

T_{RadBB} = radiant flux of a blackbody [W/m^2],

T = absolute kinetic temperature [K]

σ = Stefan-Boltzmann constant [$5.6697 \times 10^{-8} \text{ W m}^{-2} \text{ K}^{-4}$]

This equation shows that the higher the temperature of the radiating object the greater the total amount of radiation (energy) it emits. The relation is not linear; irradiance is proportional to the fourth power of the black body's temperature.

1.2.4 Wien's Displacement Law

Wien's law (Heal 2003; Walker 2008; Tipler 2000) describes the wavelength at which maximum spectral radiant exitance occurs:

$$\lambda_{\max} = \frac{A}{T} \quad (1.3)$$

λ_{\max} = wavelength of maximum spectral radiant exitance [μm]

A = Wien's constant [$2897.8 \mu\text{m K}$]

T = absolute kinetic temperature [K]

With increasing temperature of an object, its maximum exitance λ_{\max} shifts to shorter wavelengths. This can be seen in Fig. 1.5. With an average temperature of 5,778 K (5,505 °C), the sun has its peak emission in the VIS domain of the spectrum (roughly at green: 0.55 μm), while a much colder object such as the earth has its peak of emission in the TIR.

Wien's dependency of temperature and peak emission can also be observed in multispectral remote sensing data, such as depicted in Fig. 1.6 below. In the optical true color image (upper left) it can be seen that lava from Kilauea volcano is flowing to the ocean. The lava appears black, as surface crusts have already built on the lava streams, hiding the orange glowing lava under the crust. However, some parts of the lava are still incredibly hot, as can be seen in the thermal band 6 (10.4–12.5 μm) Landsat data shown in the lower right image. The white areas here represent hot areas which are much warmer than the background. Clouds clearly visible as white structures in the upper left and upper right figure appear dark in band 6 due to their low temperature. On the grey scale image of band 7 (2.09–2.35 μm) clouds appear white as reflection still plays a large role in this wavelength domain. At the same time the hottest areas of the lava appear as white structures in the central lower part of the image. These white areas are much smaller in extent than the very bright areas in band 6 and therefore depict only the very hottest regions within the lava stream, which must have temperatures well above 90 °C to stand out here (see also Table 1.2 later in this chapter).

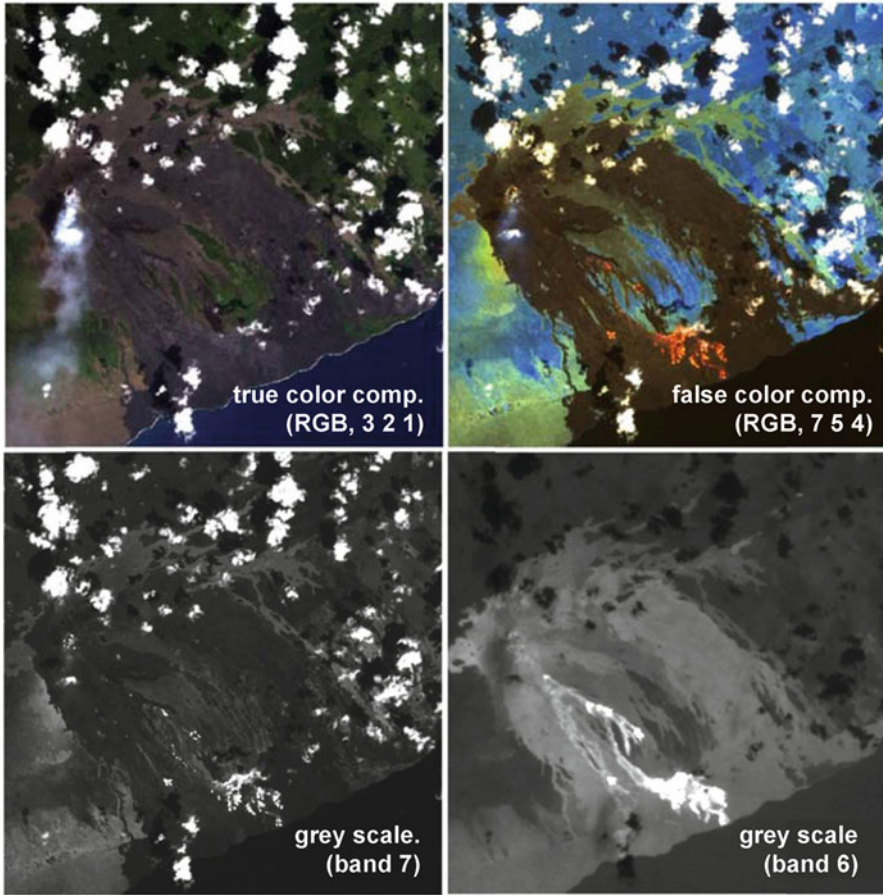


Fig. 1.6 Landsat 7 ETM+ data of Kilauea Volcano, Hawaii, USA, February 14th, 2000, *Upper left*: true color composite with the red, green and blue bands displayed in RGB; *upper right*: false color composite with the two SWIR (shortwave infrared) bands 7 and 5 and NIR band 4 displayed in RGB; *lower left*: grey scale image of shortwave infrared band 7 (2.09–2.35 μm); *lower right*: grey scale image of the thermal infrared, TIR, band 6 (10.40–12.50 μm)

1.2.5 Kirchhoff's Law and the Relevance of Emissivity

Planck's law defines the radiation released by a blackbody. Very few terrestrial surfaces act as perfect black bodies following Planck's law. Most objects emit less than predicted from their kinetic temperature. This fact is taken into account by the emissivity coefficient ($\epsilon_{(\lambda)}$). ϵ is the radiant flux of an object at a given temperature over the radiant flux of a blackbody at the same temperature. For a blackbody, all absorbed radiation is emitted again ('good absorbers are good emitters') and

Kirchhoff's law (1860) applies, stating that the emittance at a given wavelength is equal to its absorbance at the same wavelength:

$$\varepsilon_{(\lambda)} = \alpha_{(\lambda)} \quad (1.4)$$

Taking into account energy conservation, where the sum of absorption (α), reflection (ρ), and transmission (τ) equals 1, and Eq. 1.4:

$$\varepsilon_{(\lambda)} + \rho_{(\lambda)} + \tau_{(\lambda)} = 1 \quad (1.5)$$

As most objects are opaque and do not transmit radiation, Eq. 1.5 can be re-formulated as:

$$\varepsilon_{(\lambda)} + \rho_{(\lambda)} = 1 \quad (1.6)$$

Hence, the spectral emittance of an object can be calculated from its reflectance (for a blackbody), and vice versa. While materials with a high ε absorb large amounts of incident energy and radiate large quantities of energy, materials with low ε absorb and radiate lower amounts of energy (Kirchhoff 1860; Sabins 1996).

Emissivity varies depending on surface type and wavelength but is not temperature dependent (Flynn et al. 2001). Table 1.1 presents emissivities of common surfaces averaged for the wavelength range of 8–14 μm .

Based on Eq. 1.2 and the definition of emissivity, the conversion of radiance temperature to kinetic temperature is according to:

$$T_{(\text{rad})} = \varepsilon^{(1/4)*} T_{(\text{kin})} \quad (1.7)$$

Due to emissivities below 1 for real materials, the radiance temperature, $T_{(\text{rad})}$, measured by a sensor is always lower than the real kinetic (surface) temperature, $T_{(\text{kin})}$, of an object.

This is a crucial fact for thermal data analysis, as it means that objects with exactly the same kinetic temperature can differ significantly in their radiant temperature. Depending on the variability of land cover surfaces (varying geologic surfaces, moisture conditions, amounts of vegetation cover, etc.) an image has to be corrected for the emissivity effect when aiming to retrieve kinetic pixel (object) temperatures. Emissivity related radiometric divergences are especially accentuated in urban areas. As emissivities of metals (e.g., aluminium, tin or copper roofs) are extremely low, the sensed temperatures will appear much lower than the sensed temperatures of surrounding objects of the same kinetic temperature (see Figs. 1.7 and 1.8). On the other hand, water surfaces and vegetation with emissivities close to one permit a quite exact assessment of their kinetic temperature (Table 1.1).

Table 1.1 Emissivity of different surfaces in the 8–14 μm wavelength range as compiled from different sources

Surface	Emissivity at 8–14 μm
Carbon powder	0.98–0.99
Water	0.98
Ice	0.97–0.98
Plant leaves, healthy	0.96–0.99
Plant leaves, dry	0.88–0.94
Asphalt	0.96
Sand	0.93
Basalt	0.92
White paper	0.90
Wood	0.87
Granite	0.83–0.87
Polished metals, averaged	0.02–0.21
Aluminium foil	0.036

Own measurements, Lillesand et al. (2008), Sabins (1996)

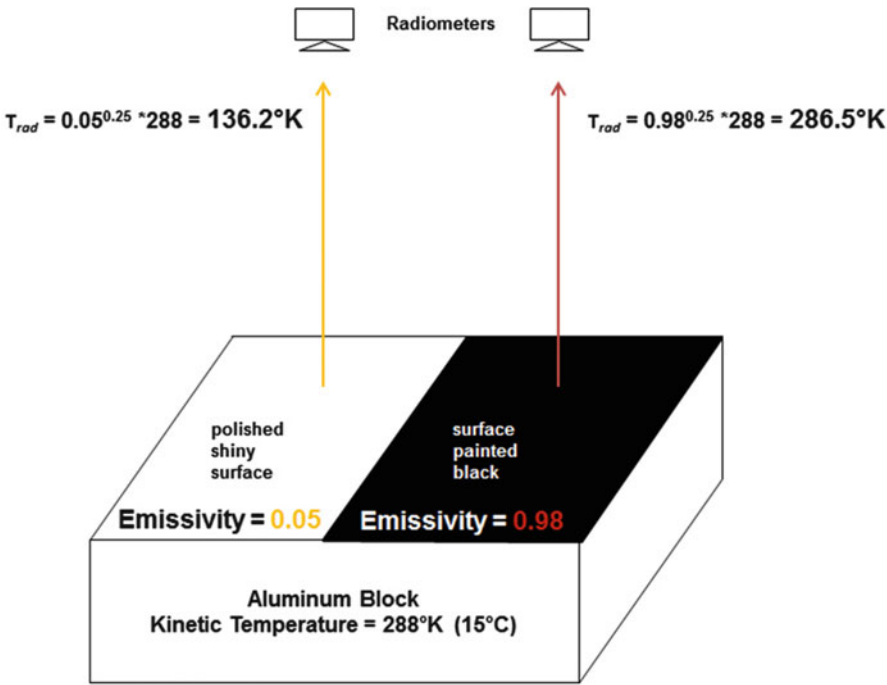


Fig. 1.7 Impact of emissivity on radiance temperature recorded at the sensor. A block of aluminium with constant kinetic temperature and very low emissivity is partially covered with a carbon-rich dark paint. Note the different temperature readings due to varying emissivities. Although the object is 15 °C, it appears as −136.8 °C on the uncovered side, and as 13.5 °C on the painted side (calculation based on Eqs. 1.2 and 1.7) (Modified after Sabins 1996)

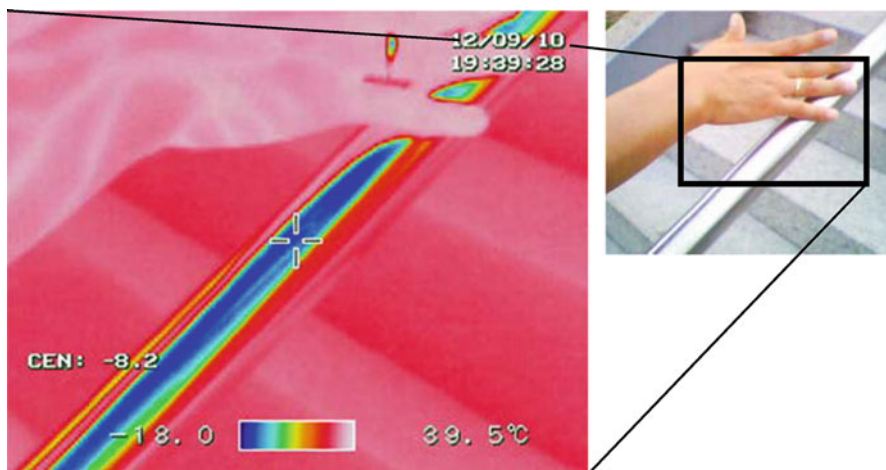


Fig. 1.8 Impact of emissivity differences on radiance temperature recorded at the sensor of a hand-held thermal camera. The picture was taken on September 10th, 2012. It shows a polished metal handrail bordering a concrete stair. Ambient air temperature at picture acquisition was around 22 °C. The human hand shows temperature values up to 37 °C. Note that even the veins within the hand can be seen as *white* (hottest) *lines*. The handrail appears at a radiance temperature of -8°C (*cross* at image center). Of course the rail is not minus 8 °C cold. However, as this picture was taken with a standard emissivity value of 1 (without emissivity correction) the handrail appears to be very cold. The same applies to the gold ring on the person's finger

1.3 Thermal Remote Sensing Data Acquisition

For thermal imaging the TIR energy radiated from an object is transferred via a scan mirror onto a detector. These detectors are usually cooled with liquid nitrogen to minimize detector-inherent noise. At the same time thermal scanners often contain controlled radiant temperature sources for calibration purposes. Details on TIR detectors can be found in Norwood and Lansing (1983). TIR detectors can be ground-based or flown on aircraft or satellites.

1.3.1 Sensitivity of Thermal Infrared Sensors

Thermal infrared sensors will be discussed in much more detail in the following chapters of this book. Here, only one example is given, based on the very commonly used spaceborne Landsat-7 Enhanced Thematic Mapper (short ETM+) sensor. All Landsat bands are acquired in either a low- or a high-gain mode spanning slightly different dynamic ranges. Gain selection is defined in the gain strategy of the Long Term Acquisition Plan (LTAP), depending on acquisition time and the dominating surface types in a scene (percentages of land, desert, ice/snow, water, sea ice, etc.).

Table 1.2 Temperature of saturation in the low- and high-gain bands of Landsat-7 ETM+

Spectral band	μm regions	Minimum temperature [$^{\circ}\text{C}$]	Maximum temperature [$^{\circ}\text{C}$]
1 (blue)	0.45–0.51	1,051 (1,075)	1,483 (1,526)
2 (green)	0.52–0.60	900 (922)	1,301 (1,340)
3 (red)	0.63–0.69	755 (775)	1,119 (1,156)
4 (NIR)	0.75–0.90	595 (613)	926 (961)
5 (MIR)	1.55–1.75	206 (217)	417 (440)
6 (TIR)	10.40–12.50	–33 (–134)	51 (77)
7 (MIR)	2.09–2.35	92 (101)	258 (276)
8 (pan)	0.52–0.90	702 (721)	1,056 (1,092)

Source: Flynn et al. (2001), modified, as in Kuenzer (2005)

These are known a priori as Landsat cover fixed frames, defined by path and row. Except for very specific requests the user has no influence on the gain setting in the reflective modes. Nevertheless, ETM+ band 6 will always be recorded and delivered in the low- and high-gain modes, extending the dynamic range of the data.

Detector saturation can occur if a surface has extremely high temperatures. Similarly, a surface will not be detected thermally if its temperature decreases below a certain threshold. Table 1.2 lists the minimum and maximum temperatures in the low-gain and high-gain (in brackets) setting, indicating the lowest or highest pixel-integrated temperature which can be detected in a certain wavelength region. It should be noted that band 6 ranges from 10.4 to 12.5 μm only, to avoid the effects of ozone adsorption. Its broad band width of 2 μm combined with only 60 m ground resolution enables a sufficient thermal energy yield. It can be seen that mid-infrared band 5 can be used to detect thermal anomalies of very high temperatures leading to saturation in band 6 (see also Fig. 1.6). Even near-infrared channel 4 offers options for the detection of extremely high temperatures. Compared to former Landsat TM (Thematic Mapper), the low- and high-gain options of ETM+ offer a higher dynamic range. Nevertheless, the thermal bands of ETM+ have proven less suitable for high temperature studies. They saturate at 51 and 77 $^{\circ}\text{C}$ respectively, while TM band 6 saturated at around 90 $^{\circ}\text{C}$. It is also often stated that ETM+ still suffers from an antiquated 8-bit dynamic range, limiting radiance steps to 256 instead of, e.g., 4096 if a 12-bit system was used (Flynn et al. 2001).

1.3.2 Daytime and Nighttime Data Acquisition

One very big advantage of TIR remote sensing is the fact that data can be acquired independent of the sun as an illumination source. So thermal data can also be acquired during the night, when remote sensing in the VIS and NIR is not possible. Several sensors can be specifically tasked to collect thermal data during the night (e.g., Aster (Advanced Spaceborne Thermal Emission and Reflection Radiometer), Landsat TM, ETM+), and some are constantly mapping the earth in the TIR range, such as MODIS (Moderate Resolution Imaging Spectroradiometer) (see Fig. 1.9), NOAA-AVHRR

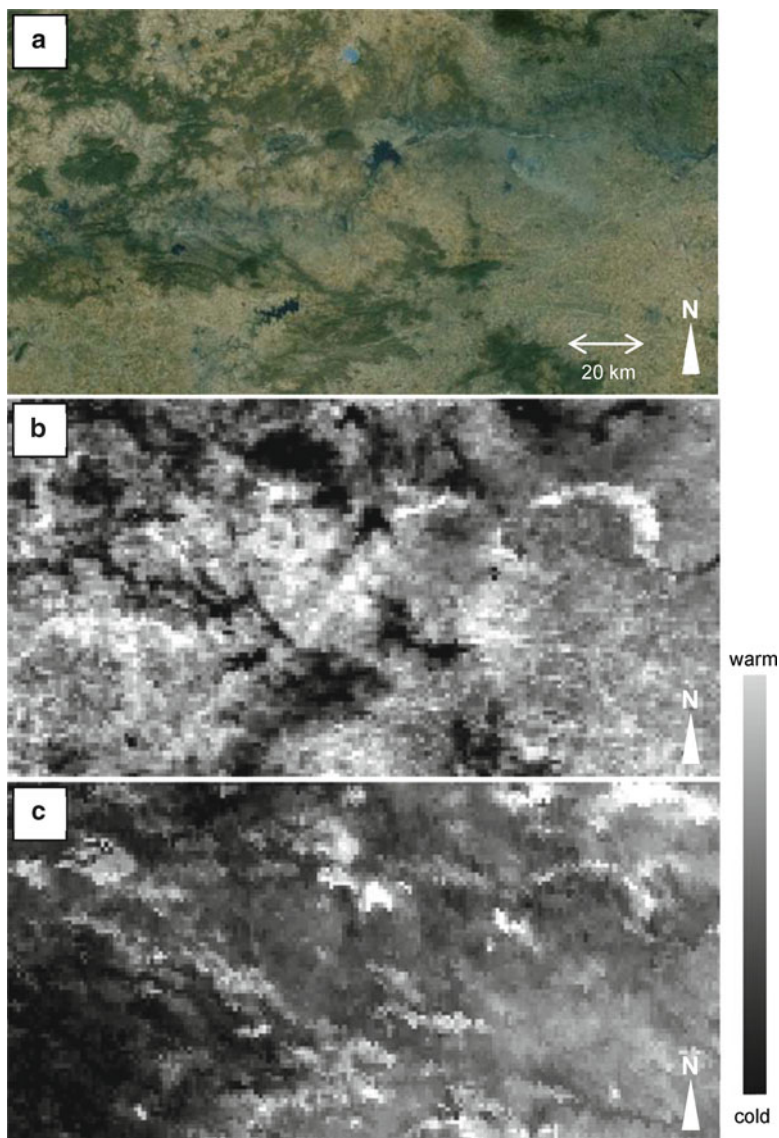


Fig. 1.9 Optical Landsat imagery (a), and daytime (morning, b) and nighttime (pre-dawn, c) thermal data acquired by MODIS in 2005 over a coal mining area in northeast India. Forested areas appear cool (bright) during the day, and warm at night; the same applies to lakes. One outstanding feature is the Jharia coal field in the *upper right part* of the image (crescent-shaped structure), which appears hot during daytime due to the low albedo and low thermal inertia of coal, and which also appears hot in pre-dawn data due to underground coal fires. The area presented covers about $230 \text{ km} \times 90 \text{ km}$. *UL* $24^{\circ}02'51\text{N}$, $84^{\circ}59'24\text{E}$, *LR* $23^{\circ}06'58\text{N}$, $86^{\circ}34'30\text{E}$

(National Oceanic and Atmospheric Administration – Advanced Very High Resolution Radiometer) or MSG SEVIRI (Meteosat Second Generation – Spinning Enhanced Visible and Infrared Imager), to name only a few.

Nighttime data is especially suitable for detecting thermal anomalies, such as hot anomalies induced by forest fires, and especially weak thermal anomalies induced by subsurface coal fires (Zhang and Kuenzer 2007; Zhang et al. 2007), peat fires, industry-related thermal water pollution, or geothermal phenomena.

Other communities, such as scientists or practitioners working in the field of model assimilation and validation, need not only one or two nighttime data sets per day, but rather nighttime as well as daytime data at dense temporal intervals covering a complete day.

During daytime uneven solar heating of the background (due to varying sun-sensor-object geometry, topography, thermal inertia) often hampers the extraction of thermally anomalous pixels, while in nighttime data – especially pre-dawn data – the solar component is much less accentuated and thermal emission of natural surfaces such as rocks, vegetation, etc. is at a minimum. Therefore, it is easier to extract anomalous pixels whose temperature is elevated independent of solar radiation. As the MODIS sensor – for example – is flown on two platforms, TERRA and AQUA, it is possible to acquire up to four thermal images of the same area within 1 day (see Fig. 1.9). Usually, data is available for the morning, afternoon, early night, and pre-dawn. This holds a large potential for multi-diurnal thermal mapping, such as presented in Kuenzer et al. (2008).

1.4 Pre-processing of Thermal Remote Sensing Data

Thermal infrared remote sensing data has to be corrected for systematic and nonsystematic geometric distortions, just like data from bands of reflective wavelengths. Usually the data is corrected simultaneously together with the reflective bands when an image stack of data is adjusted based on a data set with higher geometric accuracy, e.g., via ground control points. Details on geometric correction of image data can be found in Richards (1986).

To radiometrically correct thermal bands the physical principles of thermal absorption and emission apply. Not the reflectance in per cent has to be calculated for each pixel, but the temperature of a surface in °C or K. In a first step, sensor calibration functions are used to calculate the energy retrieved at the sensor (in $\text{W/m}^2/\text{sr}/\mu\text{m}$) from the recorded digital number, DN. The calibration functions are linear equations defined via two calibration coefficients, c_0 (offset) and c_1 (gain). The coefficients are usually frequently updated by the data providers and distributed with the raw data. Following this first step, the emitted radiance at ground level is derived. The necessary atmospheric correction takes advantage of the fact that in the thermal spectral region of 8–14 μm water vapor is the dominating disturbing parameter, while aerosols play

only a negligible role. The radiance equation in the thermal region can be expressed as:

$$L_{\text{Sat}} = L_p + \tau_v \times \varepsilon \times L_{\text{Surf}}(T) + \tau_v(1 - \varepsilon) \times F_{\text{th}}/\pi \quad (1.8)$$

With (all wavelength dependent):

L_{Sat} : at-sensor radiance

L_p : thermal path radiance

τ_v : ground to sensor atmospheric transmittance

ε : surface emissivity

T : surface temperature

L_{Surf} : blackbody radiance at the ground surface

F_{th} : thermal downwelling flux on the ground

The first term in Eq. 1.8 gives the thermal path radiance. This is thermal radiation from the atmosphere reaching the sensor having never interacted with the surface. The last term in Eq. 1.8 is the downwelling thermal radiation reflected (by the surface) back to space. The central term, finally, gives the radiation emitted by the surface of temperature (T) and transmitted to the sensor.

The equation can be resolved for T from the measured L_{Sat} , L_p , τ_v and F_{th} can be derived from atmospheric measurements or pre-calculated databases (e.g., often pre-calculated based on MODTRAN (Moderate resolution atmospheric Transmission) radiative transfer code).

Emissivity effects can be corrected approximately by classifying the optical channels of an image into different surface types and assigning an emissivity value to each land cover class. This approach is integrated in several atmospheric correction codes, such as ATCOR-3 (Atmospheric and Topographic Correction for Satellite Imagery), pre-classifying the image into three classes (water, vegetation, bare ground). Using this approach, the emissivity problem is at least approximated.

Richter (2003) and Vidal (1991) state that as a rule of thumb a 0.01 emissivity error leads to a temperature error of 0.5–1 K. Actually, the emissivity-induced error depends on the object temperature and the emissivity of the object, as demonstrated by calculations presented in Table 1.3 below. With lower emissivities temperature errors of over 10 K can be reached. For typical land cover types a 0.01 change leads to a temperature error of 0.7–1 °C. However, absolute temperature errors can be up to 25 °C, and for metal surfaces even above 100 °C (see also Figs. 1.7 and 1.8).

Therefore, detailed emissivity correction is recommended when aiming to retrieve exact surface temperatures (Becker 1987). Even if a priori classification knowledge exists, this is difficult though, since the emissivity of a pixel depends on the composition of surfaces. In case of a mixed pixel, mixed emissivities would have to be calculated. Approaches to derive the emissivity of surfaces were, amongst others, developed and applied by Becker (1987), Nerry et al. (1990), Hook et al. (1992) and Kealy and Hook (1993).

Table 1.3 Emissivity-induced temperature errors for an object of 288 K (15 °C)

Emissivity	Trad (K)	Trad (°C)	Error (from Tkin in K)	Error (for emissivity change of 0.01 in K)
0.03	119.86	−153.14	−168.14	8.94
0.04	128.80	−144.20	−159.20	7.39
0.05	136.19	−136.81	−151.81	6.35
0.06	142.54	−130.46	−145.46	5.60
0.07	148.14	−124.86	−139.86	5.03
0.08	153.17	−119.83	−134.83	4.58
0.09	157.74	−115.26	−130.26	4.21
...
0.3	213.14	−59.86	−74.86	1.75
0.31	214.90	−58.10	−73.10	1.71
...
0.7	263.43	−9.57	−24.57	0.94
0.71	264.37	−8.63	−23.63	0.93
0.72	265.29	−7.71	−22.71	0.92
...
0.97	285.82	12.82	−2.18	0.73
0.98	286.55	13.55	−1.45	0.73

1.5 Analysis of Thermal Infrared Data

There are numerous methods and approaches which are especially suitable for the analysis of TIR data; many of them being presented in the later chapters of this book. Many authors focus exclusively on the derivation of LST and SST (Baroncini et al. 2008; Eastwood et al. 2011; Freitas et al. 2010; Gleason et al. 2002; Hulley et al. 2011; Iwasaki et al. 2008; Li et al. 2004; Sobrino et al. 1994), others on sensor performance comparisons (e.g., Frey et al. 2012; Batra et al. 2006), or thermal pattern development over time (e.g., Kant et al. 2009), as well as thermal anomaly extraction (Panda et al. 2007; Kuenzer et al. 2007). A large community uses TIR data for model validation and assimilation (weather and climate models) (Jang et al. 2010; McNider et al. 1994; Pipunic et al. 2008). Furthermore, many authors utilize TIR data as additional information in multispectral data classification. Huth et al. (2012), Klein et al. (2012) and Kuenzer (2005) all have demonstrated the value of TIR data as a discriminator for certain surfaces which might not differ substantially in the VIS and NIR domain. Kuenzer (2005) for example showed that very dark coal surfaces in mining regions cannot be distinguished from fully shadowed areas in the VIS and NIR domain as both have nearly zero reflectance in all bands. However, the two can be differentiated in the TIR, as shadow areas are usually much cooler than coal surfaces, which heat up very fast during the day. However, some less known methods apart from the above exist as well, and will be introduced in the following.

1.5.1 *Considering Diurnal Temperature Dynamics: Thermal Inertia and Apparent Thermal Inertia*

Objects of the land surface and even water of the oceans all have diurnal thermal characteristics and distinct diurnal temperature curves. An object's diurnal temperature curve represents its temperature behavior over the course of a 24 h cycle. It illustrates how much and how fast an object heats up and cools down during the day. The diurnal temperature curve depends on the object's material properties (in particular its thermal inertia), season (sun-object geometry defining strength of illumination), atmospheric disturbances, and – complicating the matter for land surfaces – its exposure (aspect, slope).

Figure 1.10 illustrates the contrasting diurnal temperature variation of water and dry soil/rock. Differences mainly result from different material properties (Tipler 2000), amongst other physical parameters expressed by the thermal inertia. The thermal inertia, I ($\text{J/m}^2/\text{K/s}^{-5}$), is defined as the resistance of a material to heating. The thermal inertia is the product of three factors: the energy needed to raise the temperature of a material by 1 °C (heat capacity c) per mass unit of the substance, the density of a material, p , and the thermal conductivity, k , of the object (see also Table 1.4).

$$I = \sqrt{c \times p \times k} \quad (1.9)$$

Variations in I result in changes to ΔT (Kahle et al. 1976). ΔT is the difference between the maximum and minimum temperature occurring during a diurnal solar cycle. Low thermal inertias indicate low resistance to temperature change, resulting in a high ΔT (e.g., rocks). The opposite applies to surfaces with high thermal inertia (e.g., water).

While remote sensing does not allow for the direct derivation of thermal inertia (c , p and k can only be measured in situ), the concept still allows the impact of object characteristics (e.g., moisture of soils or vegetation) on T and ΔT to be exploited. Maximum and minimum radiant temperatures can be measured from thermal daytime and nighttime remote sensing images.

ΔT is calculated by subtracting the nighttime from the daytime temperature for corresponding ground resolution cells. Already Idso et al. (1975) investigated the potential of ΔT for soil moisture retrieval and found the data helpful for deriving soil moisture in the 0–4 cm horizon.

Later, the relationship of low ΔT for materials with a high I , and vice versa, was extended to calculate the so-called Apparent Thermal Inertia, ATI. The ATI is defined as:

$$\text{ATI} = (1 - A)/\Delta T \quad (1.10)$$

where A is the albedo of the pixel in the visible band. The albedo is included to compensate for the effect that dark materials absorb more sunlight than do light

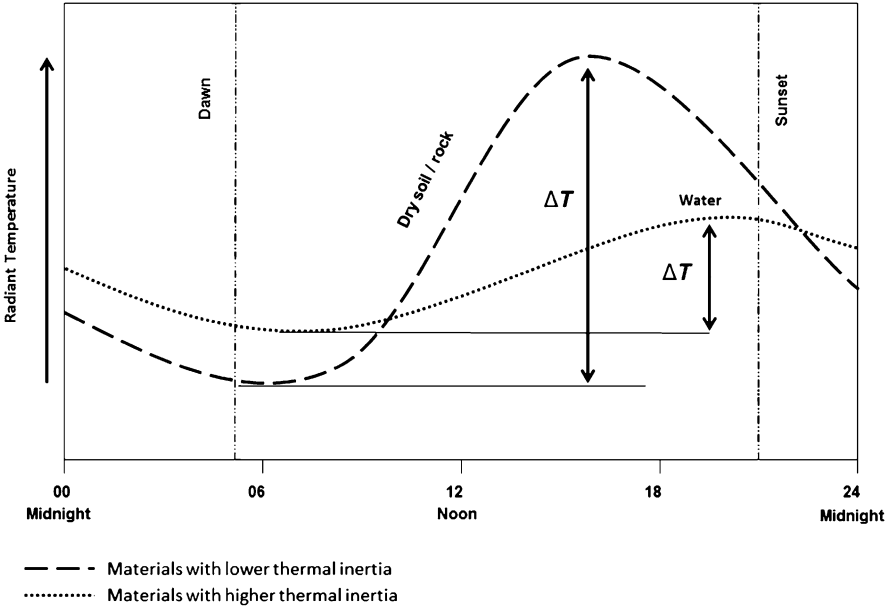


Fig. 1.10 Diurnal temperature variation of water and dry soil/rock. Each object shows a distinct diurnal temperature cycle determined by the thermal inertia of the object and the history of the incoming solar radiation (Modified from Lillesand et al. 2008)

Table 1.4 Thermal properties of geologic materials

Material	Thermal conductivity, k [W/m/K]	Thermal capacity, c [J/kg/K]	Thermal inertia, I [J/m ² /K/s ⁻⁵]
Clay soil	0.0030	0.35	0.042
Sandstone	0.0120	0.19	0.074
Limestone	0.0048	0.17	0.045
Shale	0.0042	0.17	0.041
Sandy soil	0.0014	0.24	0.024

Source: Sabins (1996)

materials. Hence, by including the term $1-A$ the effect that a dark material typically has a higher ΔT than an otherwise identical light material is somewhat compensated.

An example of ATI image utilization is shown in this book in the chapter by Notarnicola et al. (2013), who employed ATI data to qualitatively differentiate different stages of soil moisture conditions. Unlike thermal inertia, which is a fixed object-inherent value, ATI must be interpreted carefully as neither the albedo in the VIS (Bidirectional reflectance distribution function, BRDF, effects, etc.), nor ΔT are fixed. ATI, for example, cannot compensate for relief induced variations in ΔT . In an area of uniform material shadowed areas have a lower radiant temperature during the day and hence a lower ΔT than the exact same material exposed on a

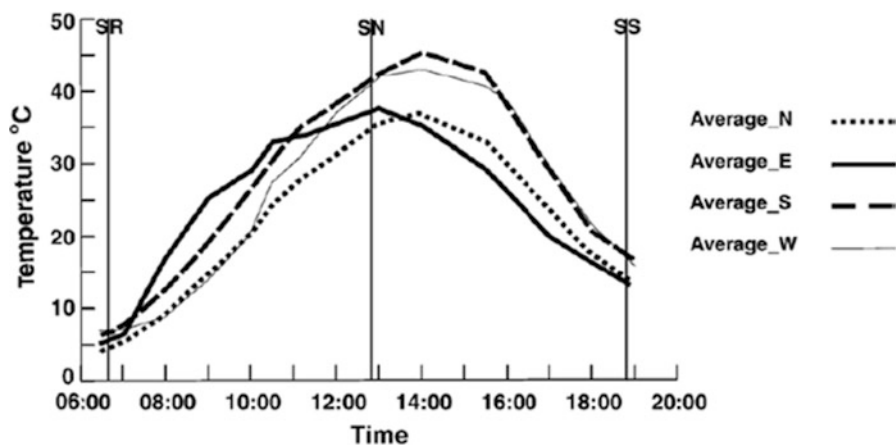


Fig. 1.11 Diurnal temperature variation of desert sand depending on different aspects (exposure to the east, south, west and north) (Source: Zhang and Kuenzer 2007)

sunlit slope. Here, topographic data and solar elevation and azimuth information have to be employed to overcome the relief-induced variation of ΔT .

Figure 1.11 depicts this increase of complexity of a diurnal temperature curve if one and the same material occurs at different aspects (thermal anisotropy). The temperatures of a small sand dune (2 m high) in the Gobi desert, China, were measured in situ at numerous points on four slopes with north, east, south and west exposition. Temperature measurements for each aspect were averaged. Measurements were recorded with a handheld radiometer at 10 min intervals and started at six AM and ended at eight PM. Figure 1.11 demonstrates the following:

- Quartz-rich desert sand reaches temperature differences of above 40 °C during a time span from 6:00 in the morning until the temperature peak is reached slightly after solar noon (SN).
- East-exposed surfaces heat faster in the morning than the other aspect directions (they are illuminated earlier)
- South- and west-exposed slopes heat up the most and stay warmer longer in the late afternoon/evening
- While peak temperature reaches only about 35 °C on east- and north-exposed slopes, temperatures of over 45 °C are reached on south and west slopes
- At e.g., a Landsat local overpass time of 10:30, temperatures of the same object/surface can differ by up to 10 °C.

To account for such effects in thermal data over land TIR imagery has to be corrected for differing solar illumination times due to varying sun-sensor-object geometries, varying sensor overpass times, and topographic (aspect, slope) effects – especially when aiming at thermal change detection or time series analysis. These corrections have to be applied in addition to several other pre-processing and correction steps: (1) sensor calibration with constantly updated calibration

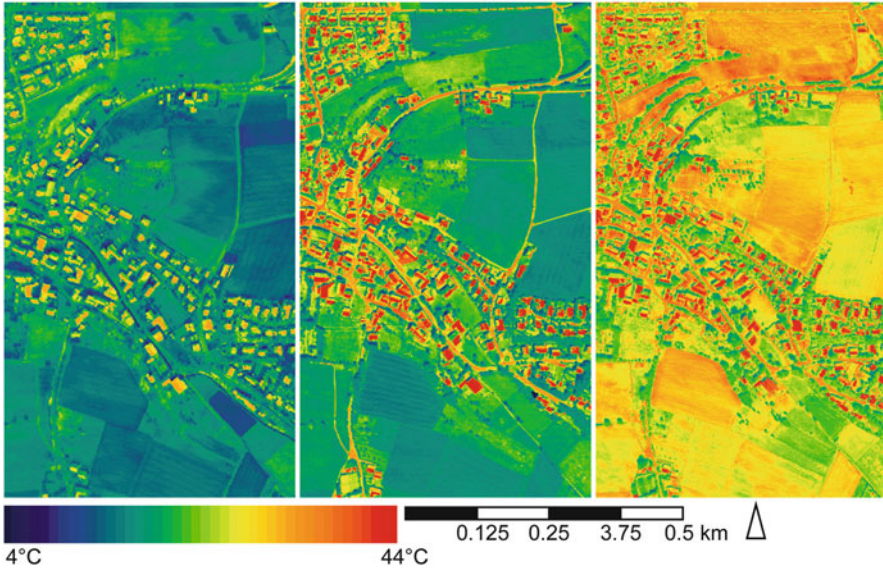


Fig. 1.12 Thermal mapping of Dahl, near Paderborn, Germany in winter (*left*), spring (*middle*), and summer (*right*), based on airborne data acquired with the DAEDALUS scanner at 300 m flight altitude. Pixel spacing is 80 cm by 80 cm (Imagery courtesy of DLR)

coefficients, (2) atmospheric corrections to retrieve object radiance, (3) emissivity corrections to receive kinetic temperature (all explained in previous sections).

1.5.2 Considering Intra-Annual Temperature Development: Implications for TIR Change Detection and Time Series Analysis

The temperature behavior of objects is not only characterized by their diurnal temperature variation within a 24 h cycle, but also by an annual temperature curve. ΔT of the 24 h cycle varies with season, and just like an average ΔT for a diurnal cycle exists, an average ΔT over the course of one year (for a specified solar time) also exists. This annual ΔT is not a ΔT derived from daytime and nighttime data, but the temperature difference of an object between an acquisition, e.g., in winter and in summer during an identical acquisition time (see Fig. 1.12).

This annual variability of temperature has to be taken into account, when time series of daytime TIR data are analyzed. Many studies investigate, e.g., so-called urban heat island effects (Schwarz et al. 2011; Streutker 2003; Tiangco et al. 2008) and some of these studies focus on the comparison of only two or a few scenes.

If one wants to derive clear indications whether a city is ‘getting hotter’ over time (usually due to increased surface sealing) one has to ensure that the data

utilized is representative (same day of year, same acquisition time, same sensor, same correction methods), also with respect to temporal coverage. The comparison of just two data sets is therefore not suitable. Instead, a time series of many scenes acquired during the same date and time should be analyzed to derive a real trend. In climate- or SST-related TIR analyses, long term time series of TIR data (e.g., 30+ years based on AVHRR data) are employed to ensure the exclusion of outlier effects and to derive solid quantitative statements.

The analysis of annual temperature variability is important for many applications such as the assessment of conditions for crop growth, the assessment of soil temperature for construction, the analysis of temperature variability impacts on building materials, or – when looking at ocean temperature – the consequences of temperature variability for nutrient loads, biodiversity, navigability, or tourism.

As a general comment, it should be noted here that thermal data – when corrected to radiance temperature in °C, and further on to kinetic temperature in °C – negative temperature (values) can occur, which is not possible for reflectance data from the VIS or NIR domain. While reflectance data is usually stored as ‘unsigned’ data (unsigned 8-bit, unsigned 12-bit etc.) thermal data should always be written as ‘signed’ (signed 8-bit, signed 12-bit, etc.) data, to allow for below 0 (negative) values.

1.5.3 Mapping Approaches Based on Varying TIR Emissivity

As already mentioned, emissivity is a wavelength-dependent term. Materials have different emissivity within the TIR domain. This means that objects have very distinct spectral signatures (spectral ‘fingerprints’) also in the TIR. The TIR spectra look similar to the continuous spectra in the VIS, NIR or MIR, and enable the distinction of materials. Sensors with multiple bands in the TIR, such as ASTER or MODIS, allow for the discriminative mapping of materials based on emissivity spectra due to differing emissivity at different wavelength in the TIR. ASTER, for example, records five thermal bands between 8.125 and 11.65 μm at 90 m spatial resolution each. Therefore, the user receives five measurements of an object’s radiant exitance in the TIR domain, and can plot a discrete emissivity spectral signature. MODIS has 36 spectral bands, of which bands 20–36 are located within the TIR domain between 3.66 and 14.385 μm . However, due to absorption bands in some of these areas, especially bands 20–23 (3.66–3.98) and bands 31 and 32 (10.78–12.27 μm) are suitable for LST and SST retrieval. Mapping approaches based on varying TIR emissivity have often been presented for geologic surface discrimination employing ASTER thermal bands (Coll et al. 2007; Haselwimmer et al. 2011).

1.5.4 Artefacts in Thermal Images

Artefacts in thermal imagery are clouds (usually very cold objects in thermal data) and cloud shadows (leading to a decrease of LST in the areas influenced by these shadows), wind smear and wind streak effects, as well as smears of high temperature events, as presented in Fig. 1.13 below.

1.5.5 Ground Truth and Validation

The accuracy of the temperatures retrieved after sensor calibration and atmospheric correction can be assessed based on ground truth temperatures (radiance and kinetic temperatures, depending on the desired final products) measured during the overflight of the airborne or spaceborne thermal sensor (Coll et al. 2005). It is then possible to measure in situ kinetic temperature directly via a contact thermometer, or without contact with the object, if its emissivity is known.

Most suitable are surfaces with a high thermal inertia (e.g., water) to prevent temperature changes during even slight temporal offsets between exact overflight time and in-situ measurement time. With water surfaces also the terrain-related (aspect, slope) uneven solar heating is omitted and its emissivity is very close to

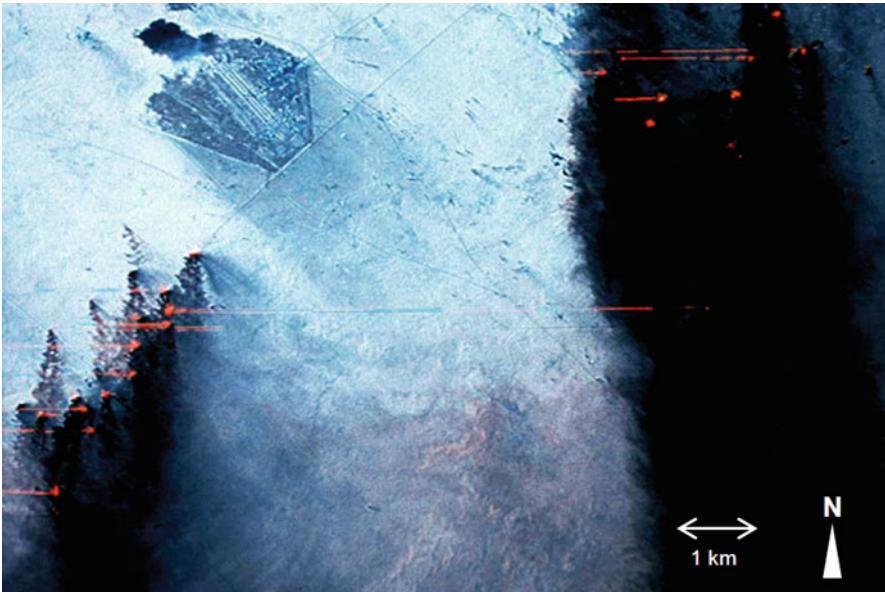


Fig. 1.13 Smear effect due to oscillating mirror motion and extreme high temperature events (burning oil and gas flares in the gulf region) can be traced all the way into the *red band* of Landsat TM imagery (Wien's displacement)

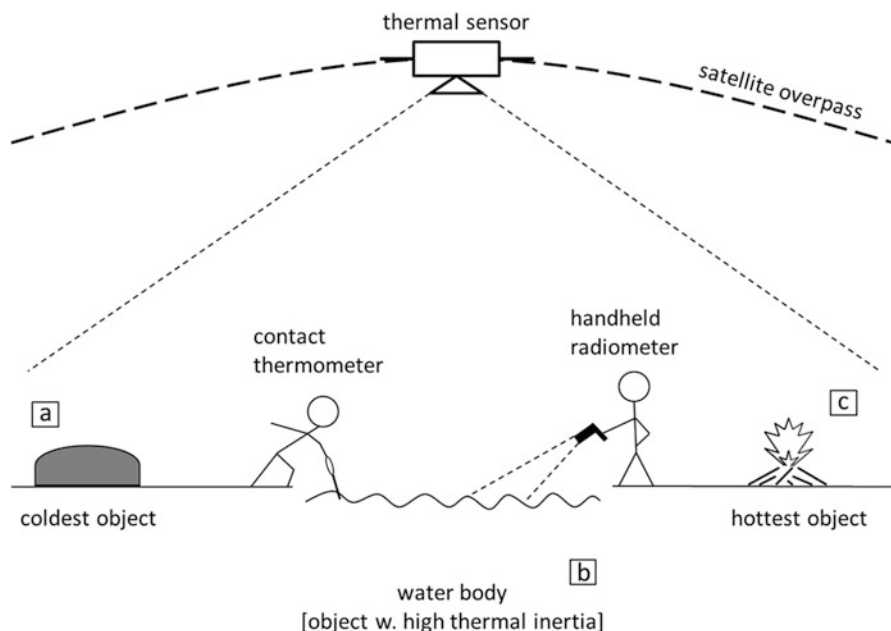


Fig. 1.14 Schematic sketch of a thermal ground truthing campaign during sensor overflight

one. At the same time, the assumedly hottest and coldest objects within the area of image acquisition should also be measured, to have ground truth for both ends of the temperature range of the data set. The measurements must all be undertaken at exact overflight time. If the objects are too far apart for one person to reach within a few minutes, several persons with several instruments need to perform the validation measurements. If, e.g., three persons measure with three radiometers and three contact thermometers, it must be ensured beforehand that these instruments are intercalibrated. Furthermore, the ground objects (e.g., water body and the hot and cold object) must be large enough to be easily recognizable in the imagery; they should each cover several image pixels (Fig. 1.14). This condition is especially difficult to meet for medium-resolution TIR data, such as from AVHRR, MODIS or MSG SEVIRI. Only few regions show homogeneous surface behavior (similar topography and roughness, same material, same reflectance, same emittance, etc.) over an area of, e.g., 5 km². If such areas are found, then one single in-situ temperature measurement will not be representative, and several measurements have to be averaged to validate one pixel (Hulley et al. 2009; Tang et al. 2010; Wan 2008).

If one aims at the validation of more than one scene (e.g., validation of time series of thermal data), then permanently installed measurement devices with temperature data loggers (e.g., in situ on the ground, in the air, etc.) usually coupled with a climate station also measuring wind speed, humidity, etc. are employed.

1.6 Conclusions

The chapter gave a short overview of the main physical principles of thermal infrared remote sensing. It also illustrated some principles behind typical applications which will be further detailed in the application chapters of this book. The interested reader is also referred to textbooks dealing with the thermal infrared domain, such as Monteith and Unsworth (2007), Sabins (1996), Jones and Vaughan (2010), Tipler (2000), and Walker (2008).

Acknowledgements The authors thank two anonymous reviewers for their valuable comments on the manuscript. Further thanks go to Clement Atzberger (BOKU, Vienna) for a critical discussion of this chapter.

References

- Baroncini F, Castelli F, Caparrini F, Ruffo S (2008) A dynamic cloud masking and filtering algorithm for MSG retrieval of land surface temperature. *Int J Remote Sens* 29(12):3365–3382
- Batra N, Islam S, Venturini V, Bisht G, Jiang L (2006) Estimation and comparison of evapotranspiration from MODIS and AVHRR sensors for clear sky days over the Southern Great Plains. *Remote Sens Environ* 103:1–15
- Becker F (1987) The impact of emissivity on the measurement of land surface temperature from a satellite. *Int J Remote Sens* 8(10):1509–1522
- Coll C, Caselles V, Galve JM, Valor E, Niclòs R, Sánchez JM, Rivas R (2005) Ground measurements for the validation of land surface temperatures derived from AATSR and MODIS data. *Remote Sens Environ* 97:288–300
- Coll C, Caselles V, Valor E, Niclòs R, Sanchez JM, Galve JM, Mira M (2007) Temperature and emissivity separation from ASTER data for low spectral contrast surfaces. *Remote Sens Environ* 110(2):162–175
- Dech SW, Tungalagsaikhan P, Preusser C, Meisner RE (1998) Operational value-adding to AVHRR data over Europe: methods, results, and prospects. *Aerosp Sci Technol* 2:335–346
- Eastwood S, Le Borgne P, Péré S, Poulter D (2011) Diurnal variability in sea surface temperature in the Arctic. *Remote Sens Environ* 115(10):2594–2602
- Flynn LP, Harris AJL, Wright R (2001) Improved identification of volcanic features using Landsat 7 ETM+. *Remote Sens Environ* 78(2):180–193
- Freitas SC, Trigo IF, Bioucas-Dias JM, Gottsche FM (2010) Quantifying the uncertainty of land surface temperature retrievals from SEVIRI/meteosat. *IEEE Trans Geosci Remote Sens* 48 (1 Part: 2):523–534
- Frey C, Kuenzer C, Dech S (2012) Quantitative comparison of the operational NOAA AVHRR LST product of DLR and the MODIS LST product V005. *Int J Remote Sens* 33(22):7165–7183
- Gleason ACR, Prince SD, Goetz SJ, Small J (2002) Effects of orbital drift on land surface temperature measured by AVHRR thermal sensors. *Remote Sens Environ* 79(2–3):147–165
- Haselwimmer CE, Riley TR, Liu JG (2011) Lithologic mapping in the Oscar II Coast area, Graham Land, Antarctic Peninsula using ASTER data. *Int J Remote Sens* 32(7):2013–2035
- Heald MA (2003) Where is the ‘Wien peak?’. *Am J Phys* 71(12):1322–1323
- Hook SJ, Gabell AR, Green AA, Kealy PS (1992) A comparison of techniques for extracting emissivity information from thermal infrared data for geologic studies. *Remote Sens Environ* 42(2):123–135

- Hulley GC, Hook SJ, Baldridge AM (2009) Validation of the North American ASTER Land Surface Emissivity Database (NAALSED) version 2.0 using pseudo-invariant sand dune sites. *Remote Sens Environ* 113(10):2224–2233
- Hulley GC, Hook SJ, Schneider P (2011) Optimized split-window coefficients for deriving surface temperatures from inland water bodies. *Remote Sens Environ* 115(12):3758–3769
- Huth J, Kuenzer C, Wehrmann T, Gebhardt S, Dech S (2012) Land cover and land use classification with TWOPAC: towards automated processing for pixel- and object-based image classification. *Remote Sens* 4:2530–2553
- Idso SB, Jackson RD, Reginato RJ (1975) Detection of soil moisture by remote surveillance. *Am Sci* 63:549–557
- Iwasaki S, Kubota M, Tomita H (2008) Inter-comparison and evaluation of global sea surface temperature products. *Int J Remote Sens* 29(21):6263–6280
- Jang K, Kang S, Kim J, Lee CB, Kim T, Kim J, Hirata R, Saigusa N (2010) Mapping evapotranspiration using MODIS and MM5 four-dimensional data assimilation. *Remote Sens Environ* 114(3):657–673
- Jones HG, Vaughan RA (2010) *Remote sensing of vegetation: principles, techniques, and applications*. Oxford University Press, Oxford, 380pp. ISBN 10: 0199207798
- Kahle AB, Gillespie AR, Goetz AFH (1976) Thermal inertia imaging: a new geological mapping tool. *Geophys Res Lett* 3(1):26–28
- Kant Y, Bharath BD, Mallick J, Atzberger C, Kerle N (2009) Satellite-based analysis of the role of land use/land cover and vegetation density on surface temperature regime of Delhi, India. *J Indian Soc Remote* 37(2):201–214
- Kealy PS, Hook SJ (1993) Separating temperature and emissivity in thermal infrared multispectral scanner data: implications for recovering land surface temperatures. *IEEE Trans Geosci Remote Sens* 31(6):1155–1164
- Kirchhoff G (1860) Ueber das Verhältniss zwischen dem Emissionsvermögen und dem Absorptionsvermögen der Körper für Wärme und Licht. *Annalen der Physik und Chemie (Leipzig)* 109:275–301
- Klein I, Gessner U, Kuenzer C (2012) Regional land cover mapping in Central Asia using MODIS time series. *Appl Geogr* 35:1–16
- Kuenzer C (2005) Demarcating coal fire risk areas based on spectral test sequences and partial unmixing using multi sensor remote sensing data. Ph.D. thesis, Technical University Vienna, Vienna, 199pp
- Kuenzer C, Zhang J, Li J, Voigt S, Mehl H, Wagner W (2007) Detection of unknown coal fires: synergy of coal fire risk area delineation and improved thermal anomaly extraction. *Int J Remote Sens* 28:4561–4585
- Kuenzer C, Hecker C, Zhang J, Wessling S, Wagner W (2008) The potential of multi-diurnal MODIS thermal bands data for coal fire detection. *Int J Remote Sens* 29:923–944
- Li F, Jackson TJ, Kustas WP, Schmugge TJ, French AN, Cosh MH, Bindlish R (2004) Deriving land surface temperature from Landsat 5 and 7 during SMEX02/SMACEX. *Remote Sens Environ* 92:521–534
- Lillesand TM, Kiefer RW (1994) *Remote sensing and image interpretation*, 3rd edn. Wiley, New York, 748pp
- Lillesand TM, Kiefer RW, Chipman JW (2008) *Remote sensing and image interpretation*, 6th edn. Wiley, New York, 768pp. ISBN 10: 0470052457
- Löffler, E (1994) *Geographie und Fernerkundung*, 3rd edn. Teubner, 251p, ISBN 3-519-13423-3. <http://www/lehmanns.de/shop/technik/183801-9783519134237-geographie-und-fernerkundung>
- McNider RT, Song AJ, Casey DM, Wetzel PJ, Crosson WL, Rabin RM (1994) Toward a dynamic-thermodynamic assimilation of satellite surface temperature in numerical atmospheric models. *Mon Weather Rev* 122:2784–2803
- Monteith J, Unsworth M (2007) *Principles of environmental physics*, 3rd edn. Academic, London, 418 pp. ISBN 10: 0125051034

- Nerry F, Labed J, Stoll MP (1990) Spectral properties of land surfaces in the thermal infrared – laboratory measurements of absolute spectral emissivity signatures. *J Geophys Res* 95 (B5):7027–7044
- Norwood VT, Lansing JC (1983) Electro-optical imaging sensors. In: Colwell RN, Simonett DS, Ulaby FT (eds) *Manual of remote sensing, 1: theory, instruments and techniques*, 2nd edn. American Society of Photogrammetry, Falls Church, pp 335–367
- Panda SK, Choudhury S, Saraf AK, Das JD (2007) MODIS land surface temperature data detects thermal anomaly preceding 8 October 2005 Kashmir earthquake. *Int J Remote Sens* 28 (20):4587–4596
- Pipunic RC, Walker JP, Western A (2008) Assimilation of remotely sensed data for improved latent and sensible heat flux prediction: a comparative synthetic study. *Remote Sens Environ* 112(4):1295–1305
- Planck M (1900) Entropie und Temperatur strahlender Wärme. *Ann Phys* 306(4):719–737
- Richards JA (1986) *Remote sensing digital image analysis – an introduction*. Springer, Berlin, 281pp
- Richter R (2003) Atmospheric and topographic correction for satellite imagery. ATCOR-2/3 User guide. Version 5.5. DLR-13 564-02/03. Wessling, 57pp
- Sabins FF (1996) *Remote sensing*, 3rd edn. Wiley, New York, 450pp
- Schwarz N, Lautenbach S, Seppelt R (2011) Exploring indicators for quantifying surface urban heat islands of European cities with MODIS land surface temperatures. *Remote Sens Environ* 115(12):3175–3186
- Sobrino JA, Li ZL, Stoll MP (1994) Improvements in the splitwindow technique for land surface temperature determination. *IEEE Trans Geosci Remote Sens* 32:243–253
- Streutker DR (2003) Satellite-measured growth of the urban heat island of Houston, Texas. *Remote Sens Environ* 85:282–289
- Tang R, Li ZL, Tang B (2010) An application of the Ts–VI triangle method with enhanced edges determination for evapotranspiration estimation from MODIS data in arid and semi-arid regions: implementation and validation. *Remote Sens Environ* 114(3):540–551
- Tiangco M, Lagmay AMF, Argete J (2008) ASTER-based study of the night-time urban heat island effect in Metro Manila. *Int J Remote Sens* 29(10):2799–2818
- Tipler PA (2000) *Physik*, 3rd edn. Spektrum Akademischer Verlag, Heidelberg, 1520pp
- Vidal A (1991) Atmospheric and emissivity correction of land surface temperature measured from satellite using ground measurements or satellite data. *Int J Remote Sens* 12(12):2449–2460
- Walker J (2008) *Fundamentals of physics*, 8th edn. Wiley, New York, 891pp. ISBN 9780471758013
- Wan ZM (2008) New refinements and validation of the MODIS land-surface temperature/emissivity products. *Remote Sens Environ* 112(1):59–74
- Zhang J, Kuenzer C (2007) Thermal surface characteristics of coal fires 1: results of in-situ measurements. *J Appl Geophys* 63:117–134
- Zhang J, Kuenzer C, Tetzlaff A, Oettl D, Zhukov B, Wagner W (2007) Thermal characteristics of coal fires 2: results of measurements on simulated coal fires. *J Appl Geophys* 63:135–147